Nonthermal fixed points in quantum field theory beyond the weak-coupling limit

Jürgen Berges[1] and Benjamin Wallisch[1,2,*]

[1]ITP, Universität Heidelberg, Philosophenweg 16, 69120 Heidelberg, Germany
[2]DAMTP, University of Cambridge, Wilberforce Road, Cambridge CB3 0WA, United Kingdom

(Received 8 October 2016; published 22 February 2017)

Quantum systems in extreme conditions can exhibit universal behavior far from equilibrium associated to nonthermal fixed points with a wide range of topical applications from early-Universe inflaton dynamics and heavy-ion collisions to strong quenches in ultracold quantum gases. So far, most studies have relied on a mapping of the quantum dynamics onto a classical-statistical theory that can be simulated on a computer. However, the mapping is based on a weak-coupling limit, while phenomenological applications often require moderate interaction strengths. We report on the observation of nonthermal fixed points directly in quantum field theory beyond the weak-coupling limit. For the example of a relativistic scalar O(N)-symmetric quantum field theory, we numerically solve the nonequilibrium dynamics employing a $1/N$ expansion to next-to-leading order, which does not rely on a small coupling parameter. Starting from two different sets of overoccupied and of strong-field initial conditions, we find that nonthermal fixed points are not restricted to parameter ranges suitable for classical-statistical simulations but extend also to couplings of order 1. While the infrared behavior is found to be insensitive to the differences in the initial conditions, we demonstrate that transport phenomena to higher momenta depend on the presence or absence of a symmetry-breaking field expectation value.

DOI: 10.1103/PhysRevD.95.036016

I. INTRODUCTION AND OVERVIEW

The existence of transient universal regimes, where even quantitative agreements between seemingly disparate physical systems can be observed, drives a remarkable convergence of research activities across traditional lines of specialization. An important class of universal scaling phenomena occurs in extreme conditions far from equilibrium, characterized by unusually strong fields or large occupancies of characteristic modes when compared to thermal equilibrium with the same energy density. Such a transient overoccupation may be found in a variety of physical applications on vastly different energy scales, ranging from (p)reheating dynamics in the early Universe [1–3] to the initial stages of relativistic heavy-ion collisions [4–7], and strong quenches in ultracold quantum gas experiments [8–10]. Important universality classes out of equilibrium have been recently discovered in these cases, providing exciting new links between the dynamics of cold gases and hot plasmas [11].

So far, most quantitative results rely on the presence of a sufficiently weak coupling parameter. In this case, essential aspects of the many-body quantum dynamics of strong fields or highly occupied modes can be mapped onto a classical-statistical field theory problem [1,12,13], which can be solved on a computer. Since universal phenomena are insensitive to details of the underlying system parameters, such as values of couplings or precise initial conditions for the subsequent evolution, one may hope that similar results persist beyond the weak-coupling limit. A corresponding fact is well known for universal scaling properties in thermal equilibrium near phase transitions associated to renormalization group fixed points, where systems with very different microscopic interaction strengths exhibit common macroscopic properties. Whether such a statement can also be made for universal scaling phenomena far from equilibrium near nonthermal fixed points, associated to turbulent transport phenomena, is a question of utmost phenomenological relevance. First indications come from holographic strong-coupling methods applied to superfluids [14,15]. It is the main objective of this work to provide an explicit example, where this question can be answered directly in quantum field theory beyond the weak-coupling limit.

Motivated by the phenomenology of heavy-ion collision experiments, where the relevant gauge coupling at early times is expected to be neither particularly small nor large, there is a series of studies trying to understand extreme conditions far from equilibrium beyond the limit of weak interactions. Classical field simulations have been employed in Refs. [16–18] for gauge field and scalar field theories at larger couplings. They seem to demonstrate the absence of any transient dynamical scaling regime by showing a rapid approach to a thermal-like Rayleigh-Jeans distribution [16] or fast isotropization for expanding systems [17,18]. However, it has been shown in Refs. [19,20] that one exceeds the range of validity of the classical descriptions for the larger couplings employed: a spurious decay of the

*b.wallisch@damtp.cam.ac.uk

quantum vacuum into propagating particle modes is observed, which then dominate the thermalization or isotropization dynamics.

Another approach employs effective kinetic descriptions. Kinetic theory can describe the long-time behavior of quantum systems if the typical occupancies are not too large and if their typical momenta are much larger than the in-medium screening scale. While the applicability of the perturbative kinetic theory requires a sufficiently weak coupling parameter, recent extrapolations beyond the weak-coupling limit in the context of heavy-ion collisions achieve a remarkable consistency with phenomenological expectations [21]. If applied to stronger interaction strengths, the kinetic descriptions show significant deviations from the known classical-statistical scaling behavior in the weak-coupling limit for gauge fields [21] as well as scalar field theory [22] because of the additional quantum corrections that now become of the same order as the classical contributions in the perturbative description. It remains an important open question whether these corrections are reliably estimated if applied at stronger couplings.[1]

In order to be able to judge the validity of extrapolations beyond the weak-coupling limit, a description of the dynamics based on a nonperturbative expansion parameter would be extremely valuable. For N-component scalar quantum field theories, this is indeed possible based on a systematic large-N expansion, which has a long history for the description of scaling phenomena. At next-to-leading order (NLO) in a resummed large-N expansion based on the two-particle irreducible (2PI) effective action [24,25], the approach is already known to analytically describe well the self-similar scaling solutions of nonthermal fixed points in the weak-coupling limit [10,26]. However, to extend to stronger interactions, a numerical evaluation seems mandatory. In particular, we are not only interested in the scaling solution itself but also want to answer the question for what range of couplings a nonthermal fixed point is approached from generic strong-field or overoccupied initial conditions. While the nonthermal fixed point is known to have attractor properties in the limit of weak couplings, such that no fine-tuning of initial conditions or parameters is required to approach it, this is not guaranteed at stronger couplings even if the fixed point solution itself would still exist.

In this work, we present a numerical solution of the time evolution equations at NLO in the $1/N$ expansion of a self-interacting O(N)-symmetric quantum field theory in $3+1$ space-time dimensions without expansion. Because of the non-Markovian nature of the evolution equations, it is very demanding to go beyond the earlier times considered in previous studies [3]. This is achieved in this work through algorithmic and computational advances, which allow us for the first time to study the approach to nonthermal fixed points and the subsequent deviation evolution toward thermal equilibrium. The latter is not accessible in classical-statistical descriptions even at weak couplings because of the Rayleigh-Jeans divergence of classical field theory.

One of the main results of this work is that, even for couplings of order 1, we find the transient universal scaling results as observed before from classical-statistical simulations in the weak-coupling limit. Remarkably, the scaling behavior for infrared momentum modes is found to persist even for much stronger interaction strengths, while the lower-occupied higher momentum modes deviate from scaling in this case. In general, scaling is seen to hold only in momentum regimes with modes having occupancies larger than 1. Once the characteristic occupancies drop below 1 at later times, the approach to a Bose-Einstein distribution is observed as expected. Although our results on the presence and relevance of nonthermal fixed points beyond the weak-coupling limit seem to be in conflict with extrapolated kinetic theory expectations, our findings are in line with corresponding facts known from universal scaling phenomena in thermal equilibrium.

This paper is organized as follows. In Sec. II, we discuss the evolution equations beyond the weak-coupling limit and the employed initial conditions. Sections III and IV cover the results for (a) overoccupied and (b) strong-field initial conditions, respectively. It is shown that the particle cascade toward the infrared is insensitive to the different initial conditions employed, while the energy cascade toward higher momenta depends on the presence or absence of a symmetry-breaking field expectation value. The energy cascade for the symmetric case with a vanishing field expectation value is observed here to emerge from the nonequilibrium evolution for the first time. We also compare to the classical-statistical field theory limit and demonstrate the decay of the quantum-half for strong enough couplings as an artifact of classical approximations applied beyond their range of validity. Section V concludes with a summary. In a set of Appendixes, we review the equations of motion from the $1/N$ expansion of the 2PI effective action (Appendix A), describe the performed mass renormalization (Appendix B), and provide the energy-momentum tensor (Appendix C) for completeness.

II. EVOLUTION EQUATIONS BEYOND THE WEAK-COUPLING LIMIT

A. Large-N expansion to NLO

We consider a relativistic O(N)-symmetric real N-component scalar field theory with quartic self-interaction

[1]For the extrapolation to stronger couplings, it would be important to resolve also some puzzling questions that remain even in the weak-coupling limit since kinetic descriptions for longitudinally expanding systems apparently fail to reproduce some relevant results of classical-statistical simulations, such as the ratio of longitudinal to transverse pressure characterizing isotropization for longitudinally expanding systems in the regime where both are expected to have an overlapping range of validity [23].

in $3+1$-dimensional Minkowski space-time. The N-component field theory often serves in paradigmatic models to describe early-Universe inflaton dynamics. For $N=4$, the symmetry group employed is locally isomorphic to a chiral $\mathrm{SU}_L(2)\times\mathrm{SU}_R(2)$ symmetry relevant in the context of low-energy effective descriptions of quantum chromodynamics. In addition, the O(4) model also reflects the field content of the Higgs sector of the Standard Model of particle physics. Since we anticipate nonrelativistic dynamics at sufficiently low momenta [10], there is also a direct correspondence to quantum Gross-Pitaevskii models for a single charged Bose field for $N=2$, for example.

As we aim to go beyond the weak-coupling limit, we take into account quantum corrections according to their scaling with the number of field components N. Here, $1/N$ is the (small) expansion parameter, which is not an expansion in powers of the coupling parameter. As a consequence, the $1/N$ expansion is not restricted to weak interactions in general and has been successfully employed also in nonperturbative contexts, such as the description of critical phenomena [27]. Moreover, the resummed $1/N$ expansion based on the 2PI effective action employed is known to exhibit improved convergence properties for the computation of thermal scaling phenomena [28] and the resummation of secular terms required to describe the long-time behavior of quantum fields out of equilibrium [24].

The classical Lagrangian density for the massless field theory reads[2]

$$\mathcal{L}[\varphi]=\frac{1}{2}\partial_\mu\varphi_a\partial^\mu\varphi_a-\frac{\lambda}{4!N}(\varphi_a\varphi_a)^2 \tag{1}$$

with the field components $\varphi_a(x)$ and coupling parameter λ. Summation over repeated field space indices $a=1,\ldots,N$ as well as Lorentz indices $\mu=0,1,2,3$ is implied. For the corresponding classical equations of motion,

$$\left(\partial_\mu\partial^\mu+\frac{\lambda}{6N}\varphi^2(x)\right)\varphi_a(x)=0 \tag{2}$$

with $\varphi^2\equiv\varphi_a\varphi_a$, one can always scale out the dependence on the coupling by introducing a rescaled field,[3]

$$\varphi_a(x)\to\frac{1}{\sqrt{\lambda}}\varphi_a(x). \tag{3}$$

The rescaled classical field obeys the evolution equation

$$\left(\partial_\mu\partial^\mu+\frac{1}{6N}\varphi^2(x)\right)\varphi_a(x)=0, \tag{4}$$

and, as a consequence, in classical(-statistical) dynamics, any dependence on the coupling only enters via the initial conditions for the solution of the differential equation (4).

In contrast, the coupling cannot be scaled out from the corresponding quantum dynamics, where the classical field $\varphi_a(x)$ is replaced by a Heisenberg field operator $\hat{\varphi}_a(x)$. The quantum description is crucial, for example, to overcome the Rayleigh-Jeans divergence of classical-statistical field theory [24].

However, simple approximations may not reflect this distinctive property of the quantum theory. For instance, at leading order (LO) in the expansion in powers of $1/N$, the quantum expectation value of the field operator,

$$\phi_a(x)\equiv\langle\hat{\varphi}_a(x)\rangle, \tag{5}$$

obeys—after a rescaling corresponding to (3)—the evolution equation [25]

$$\left(\partial_\mu\partial^\mu+\frac{1}{6N}[\phi^2(x)+F(x,x)]\right)\phi_a(x)=0 \tag{6}$$

with $\phi^2\equiv\phi_a\phi_a$. In comparison to the classical evolution equation (4), the extra term $F(x,x)\equiv F_{aa}(x,x)$ in (6) stems from the connected part of the *anticommutator* expectation value of two Heisenberg field operators,

$$F_{ab}(x,y)\equiv\frac{1}{2}\langle\{\hat{\varphi}_a(x),\hat{\varphi}_b(y)\}\rangle-\phi_a(x)\phi_b(y). \tag{7}$$

This anticommutator or so-called statistical two-point function obeys at LO a similar equation as the field expectation value [25]:

$$\left(\partial_\mu\partial^\mu+\frac{1}{6N}[\phi^2(x)+F(x,x)]\right)F(x,y)=0. \tag{8}$$

Accordingly, no dependence on the coupling parameter λ appears in the evolution equations for the rescaled quantum field at LO in a large-N expansion.

This changes at NLO in the $1/N$ expansion, where the evolution equations start to depend explicitly on the *commutator* expectation value [24,25]

$$\rho_{ab}(x,y)=\mathrm{i}\langle[\hat{\varphi}_a(x),\hat{\varphi}_b(y)]\rangle. \tag{9}$$

The spectral function (9) encodes the equal-time commutation relation of the quantum theory,

$$\partial_{x^0}\rho_{ab}(x,y)|_{x^0=y^0}=\delta_{ab}\delta(\mathbf{x}-\mathbf{y}), \tag{10}$$

and the somewhat lengthy evolution equations at NLO are given in Appendix A in detail.

For the purpose of the present discussion, the characteristic dependence on the coupling parameter entering at NLO can be illustrated by the "one-loop" self-energy term

[2]We use the Minkowski metric with signature $(1,-1,-1,-1)$, the notation $x=(x^0,\mathbf{x})$ for time $x^0=t$ and spatial coordinates $\mathbf{x}$, and units where the speed of light, the reduced Planck constant, and Boltzmann's constant equal unity, $c=\hbar=k_\mathrm{B}=1$.

[3]The same can be done also for a massive classical scalar field.

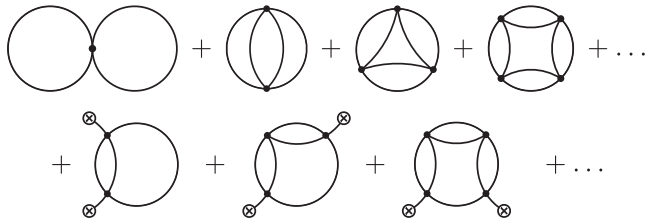

FIG. 1. Diagrammatic representation of the infinite series of contributions to the free energy density at NLO in the $1/N$ expansion of the 2PI effective action. The lines denote self-consistent propagators, solid circles denote vertices, and crosses denote field expectation values.

$$\Pi_F(x,y) = \frac{1}{6N}\left[F^2(x,y) - \left(\frac{\lambda}{2}\right)^2 \rho^2(x,y)\right] \tag{11}$$

with $F^2 \equiv F_{ab}F_{ab}$ and $\rho^2 \equiv \rho_{ab}\rho_{ab}$. This self-energy term represents an essential building block of the infinite number of one-loop-type "ring diagrams" appearing at NLO in the large-N expansion, as indicated for the example of the free energy density or 2PI effective action in Fig. 1.

The commutator term $(\lambda/2)^2\rho^2$ in (11) encodes the genuine coupling dependence entering the NLO evolution equations. In fact, implementing the $1/N$ expansion to NLO in the corresponding classical-statistical theory, one can check that the commutator term is absent classically, while the F^2-term in (11) has a classical analog [13]. This reflects the fact that classical-statistical approximations for the description of quantum dynamics require sufficiently weak couplings, such that contributions from the $(\lambda/2)^2\rho^2$-term are sufficiently small compared to those from the F^2-term. Accordingly, by solving the quantum evolution equations, one expects to confirm characteristic results known from classical-statistical simulations in the weak-coupling limit for the same initial conditions, while this may not be expected at sufficiently large values of λ.

B. Initial conditions

We consider spatially homogeneous and isotropic initial conditions. As a consequence, the macroscopic field (5) only depends on time $t, \phi_a(t)$, and the correlation functions depend on times and relative spatial coordinates, $F_{ab}(t,t',|\mathbf{x}-\mathbf{y}|)$ and $\rho_{ab}(t,t',|\mathbf{x}-\mathbf{y}|)$. The initial macroscopic field is chosen to point in a given direction in field index space as $\phi_a = \phi\delta_{a1}$, which is preserved by the nonequilibrium dynamics of the O(N)-symmetric quantum theory. Accordingly, we can take the two-point functions to be diagonal with one longitudinal and $N-1$ transverse parts, i.e., $(F_{ab}) = \mathrm{diag}\{F_\parallel, F_\perp, \ldots, F_\perp\}$ and $(\rho_{ab}) = \mathrm{diag}\{\rho_\parallel, \rho_\perp, \ldots, \rho_\perp\}$.

The initial size of the rescaled macroscopic field, $\phi_0 \equiv \phi(t=0)$, will be characterized by σ_0 defined as

$$\sigma_0 = \frac{\phi_0}{\sqrt{6N}}, \tag{12}$$

while the time derivative of the field is taken to vanish at initial time $t = 0$. Apart from initial conditions with a large macroscopic field, we consider the case of an initially highly occupied gas of free particles with characteristic (highest) momentum Q. More precisely, a class of initial conditions for the anticommutator two-point function will be described in spatial Fourier space with 3-momentum $\mathbf{p}$ as

$$F_{\parallel,\perp}(t=t'=0,|\mathbf{p}|) = \frac{n_0\Theta(Q-|\mathbf{p}|)+\lambda/2}{\omega_{\parallel,\perp}(0,|\mathbf{p}|)} \tag{13}$$

with occupancy parameter n_0, Heaviside step function Θ and initial dispersion

$$\omega_{\parallel,\perp}(0,|\mathbf{p}|) = \sqrt{\mathbf{p}^2 + M^2_{\parallel,\perp}(0)}. \tag{14}$$

Here, $M_{\parallel,\perp}(0)$ denotes the initial renormalized in-medium mass of longitudinal and transverse modes, respectively (cf. Appendix B).

Taking into account that we have performed a field rescaling according to (3), the actual initial occupancy per mode, $f(t=0,|\mathbf{p}|)$, is given by

$$f(t=0,|\mathbf{p}|) = \frac{n_0}{\lambda}, \qquad |\mathbf{p}| \le Q \tag{15}$$

according to (13). This initial occupancy is supplemented by the quantum-half which appears as $\lambda/2$ in the initial correlator (13) for the rescaled field. For large typical occupancy n_0/λ, the function (15) clearly represents a far-from-equilibrium distribution, in sharp contrast to a thermal (Bose-Einstein) distribution where the characteristic occupancy is $\mathcal{O}(1)$ for momenta of order the temperature.

Neglecting $M_{\parallel,\perp}(0)$ for a moment, the total initial energy density ϵ_0 is approximately given by

$$\epsilon_0 \simeq \frac{3}{2}\frac{N}{\lambda}\sigma_0^4 + \frac{n_0}{8\pi^2}\frac{N}{\lambda}Q^4. \tag{16}$$

In contrast to the contribution $\sim N\sigma_0^4/\lambda$ from the macroscopic field, the relativistic gas contribution $\sim NQ^4/\lambda$ comes with a significant suppression factor $(8\pi^2)^{-1}$ unless we consider initial occupancy parameter values of order $n_0 = 100$. In the following, the latter value will be employed for n_0, which is also in line with similar choices in studies employing classical-statistical lattice simulations (see, e.g., Ref. [10]).

We will consider two generic types of initial condition scenarios here, which are frequently considered in the literature: (a) fluctuation initial conditions with $n_0 \neq 0$ and $\sigma_0 = 0$ and (b) macroscopic field initial conditions with $\sigma_0 \neq 0$ in the presence of vacuum fluctuations, i.e. with $n_0 = 0$. This is schematically depicted in Fig. 2.

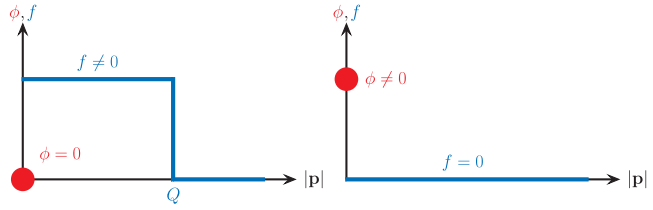

(a) Fluctuation initial condition. (b) Macroscopic field initial condition.

FIG. 2. Illustration of the employed initial condition scenarios.

The macroscopic field initial condition (b), which is also referred to as the strong-field initial condition, is known to lead to the phenomenon of parametric resonance at early times, which has been studied by the techniques employed here in Ref. [29]. The parametric resonance instability quickly leads to large occupancies in a characteristic momentum range, similar to what is considered with the fluctuation initial condition (a), which is also known as the overoccupied initial condition. However, there is an important difference: while in scenario (b) the presence of a nonzero field expectation value singles out an initial direction in field index space such that the O(N) symmetry is not manifest, scenario (a) proceeds entirely in the symmetric regime because the initially vanishing field expectation value and time derivative remain identically zero at all times by virtue of the O(N) symmetry. In particular, a nonzero macroscopic field is known to induce effective cubic self-interactions even though the Lagrangian (1) only exhibits quartic interactions. We will analyze the impact of the underlying different scattering processes for scenarios (a) and (b) in the subsequent Secs. III and IV, respectively.

We consider the time evolution of systems that start far away from thermal equilibrium. Stated differently, initially—or after a characteristic short time starting from macroscopic field initial conditions [29]—the typical occupancy is much larger than in thermal equilibrium, i.e. $f \sim n_0/\lambda \gg 1$. For $n_0 = 100$, this already limits the maximum value of the coupling parameter to be $\lambda \lesssim \mathcal{O}(10)$, which we will not exceed in our study. In turn, starting far from equilibrium with $n_0/\lambda \gg 1/2$, the quantum corrections are expected to play no significant role at initial times. In contrast, quantum corrections become relevant at later times when the typical occupancy decreases as the system evolves on its way toward thermal equilibrium. The stronger the coupling, the earlier these quantum corrections are expected to set in. Here, an important question is to find out up to what coupling strength the system still approaches a transient nonthermal fixed point, as is known to occur in the weak-coupling limit, before the quantum corrections lead to thermal equilibrium asymptotically.

Numerical results will be presented for $N = 4$, and we will cover a coupling range of $10^{-2} \leq \lambda \leq 10$ for a cutoff-regularized theory. More precisely, we perform a self-consistent mass renormalization at initial time as detailed in Appendix B and verify that the results are insensitive to variations of the employed ultraviolet momentum cutoff. For the field initial condition, we take $M_{\parallel}^2(0)/\sigma_0^2 \approx 3$ and $M_{\perp}^2(0)/\sigma_0^2 \approx 1$, and for the fluctuation initial condition, $M^2(0)/Q^2 \approx 0.43$ for all coupling values we consider. All results are checked also for possible infrared cutoff effects and found to be stable.

The computations are performed in momentum space on an isotropic grid. In order to be able to reach sufficiently large times, we adapt discretizations as a function of time. While the computations are done for different sets of discretization parameters to check convergence, results shown for fluctuation (field) initial conditions for times $Qt \leq 1200$ ($\sigma_0 t \leq 1200$) are from computations on a spatial grid characterized by $N_s = 540$ points with a grid spacing $Qa_s = 0.4$ ($\sigma_0 a_s = 0.5$). Subsequently, we reduce the number of grid points to $N_s = 135$ ($N_s = 225$), thereby increasing the infrared cutoff. We checked that the spectra lie on top of each other in the common momentum range for overlapping times. In general, the temporal grid at early times has to be finer than at later times in order to resolve the initially faster processes such as instabilities as compared to the subsequent slow power-law behavior near nonthermal fixed points. For the displayed results, we changed from $Qa_t = 0.08$ ($\sigma_0 a_t = 0.15$) for early times to $Qa_t = 0.16$ ($\sigma_0 a_t = 0.30$) at $Qt = 160$ ($\sigma_0 t = 225$). For field initial conditions at stronger couplings $\lambda \gtrsim 1$, it turned out that it is sufficient to use $N_s = 225$ at all times; however, we employed smaller step sizes changing from $\sigma_0 t = 0.10$ to 0.20 at $\sigma_0 t = 150$.

III. RESULTS STARTING FROM FLUCTUATION INITIAL CONDITIONS

A. Distribution and dispersion relation

We first consider the dynamics in the symmetric regime starting from the fluctuation initial condition (a) of Sec. II B. In order to discuss the nonequilibrium time evolution, it is convenient to extract a time-dependent particle number distribution $f(t, |\mathbf{p}|)$, which can be defined in terms of the equal-time statistical two-point function (7) in spatial Fourier space as [24]

$$\frac{f(t,|\mathbf{p}|) + 1/2}{\omega(t,|\mathbf{p}|)} = \lambda^{-1} F(t,t,|\mathbf{p}|). \tag{17}$$

At time $t = 0$, this definition coincides with (13) for the initial dispersion (14). In practice, we extract a time-dependent distribution function and dispersion relation in accordance with (17) by employing

$$f(t,|\mathbf{p}|) + \frac{1}{2} = \lambda^{-1} \sqrt{F(t,t',|\mathbf{p}|)\partial_t \partial_{t'} F(t,t',|\mathbf{p}|)}|_{t=t'}, \tag{18}$$

$$\omega(t,|\mathbf{p}|) = \sqrt{\partial_t \partial_{t'} F(t,t',|\mathbf{p}|)/F(t,t',|\mathbf{p}|)}|_{t=t'}. \tag{19}$$

In general, there is, of course, no unique definition of a mode particle number in the interacting theory. Nevertheless, we will use the notion of a distribution function to illustrate our results, remembering that one can always think of the well-defined correlation functions on which our definitions are based.

B. Nonthermal fixed points

The distribution function for different values of the coupling $\lambda = 0.01$, 0.1, and 1 is presented in Fig. 3 at different times, which show the evolution starting from the displayed initial overoccupied state. One observes the emergence of two distinct regimes for small ($|\mathbf{p}| \lesssim 0.3Q$) and for larger momenta ($|\mathbf{p}| \gtrsim 0.3Q$). The evolution is self-similar [10], and the approximate power-law behavior corresponds to an inverse particle cascade toward the infrared [3,30] and a direct energy cascade toward larger momenta [31]. This is the first time that the dual cascade has been observed to emerge in a quantum field theoretical calculation without relying on the classical-statistical approximation.

In fact, the scaling exponent for the direct energy cascade at higher momenta is found to be well approximated by

$$\kappa_{\mathrm{E}} = 5/3, \tag{20}$$

which is the value predicted by analytical considerations in the framework of kinetic theory with two-to-two scattering in the absence of a macroscopic field expectation value ($\phi = 0$) [31]. The energy cascade exponent (20) has not been observed before from classical-statistical simulations. The latter see also a direct energy cascade, however, with an expected exponent $3/2$ characterizing the scattering of a particle off a macroscopic field mode [31] (cf. also Sec. IV below).

The possibility to observe (20) is due to the fact that we are able to preserve the O(N) symmetry at all times by setting the initial field $\phi(t = 0)$ as well as its time derivative to zero. In contrast, classical-statistical simulations always start with nonzero values for the field or its time derivative. A vanishing macroscopic field average can then only be obtained by sampling over many individual runs; however, the initial bias cannot be set to zero identically with that procedure. The situation is similar to the well-known phenomenon of spontaneous symmetry breaking in thermal equilibrium, where a small bias can lead to the appearance of a macroscopic field value.

The inverse particle cascade at low momenta is well approximated by a power law with exponent

$$\kappa_{\mathrm{N}} = 5 \tag{21}$$

as displayed by the gray dashed line in all three panels of Fig. 3. The value of this exponent is characteristic for a nonrelativistic inverse particle cascade toward the infrared [8,10]. The appearance of the nonrelativistic infrared regime within the relativistic field theory is a consequence of the presence of an effective mass gap, which has been pointed out in Ref. [10]. Indeed, we see in Fig. 4 that the

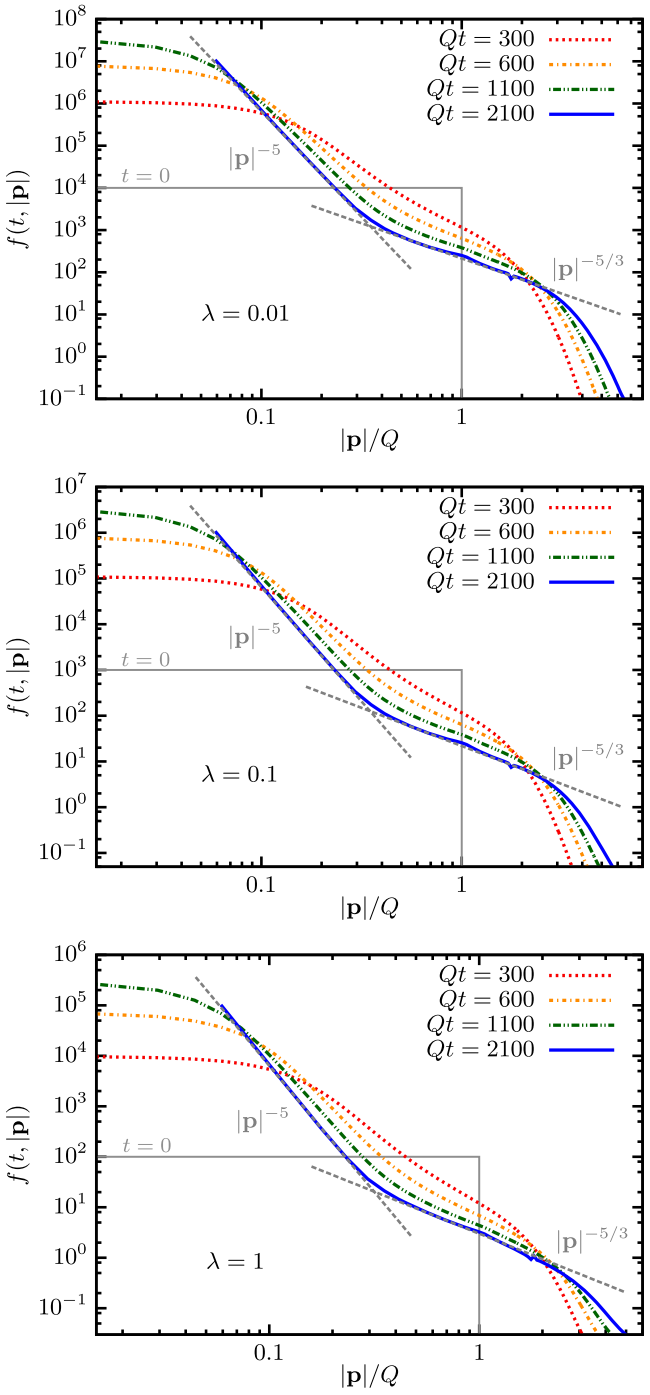

FIG. 3. Particle number distribution for fluctuation initial conditions with $\lambda = 0.01$, 0.1, 1 (*top* to *bottom*) at different times including the initial time (gray). The approximate power laws with exponents $\kappa_{\mathrm{N}} = 5$ and $\kappa_{\mathrm{E}} = 5/3$ characterize the dual cascade in the respective momentum ranges (dashed gray lines).

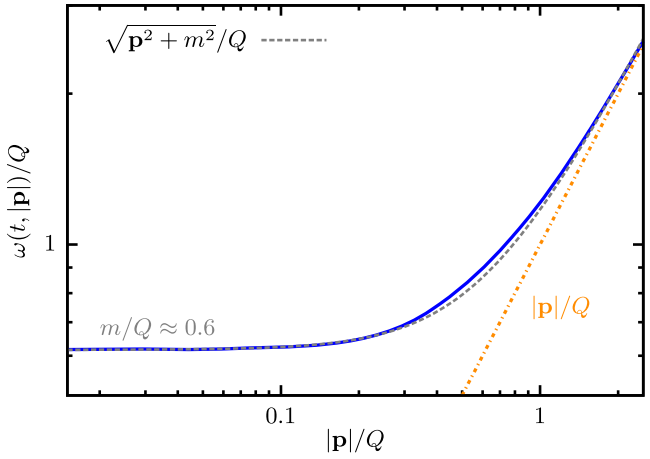

FIG. 4. Dispersion relation for fluctuation initial conditions with $\lambda = 0.01$ at $Qt = 1200$ exhibiting an effective mass gap m. A fit to the quasiparticle dispersion relation $\sqrt{\mathbf{p}^2+m^2}$ is performed in good agreement with the numerical data for $m/Q \approx 0.6$. Additionally, a linear dispersion relation, $\omega = |\mathbf{p}|$, is shown for comparison.

dispersion relation (19) is approximately constant in the momentum range where we observe the power law in the infrared. We also show a linear dispersion relation as expected for relativistic momenta. In addition, we fit a quasiparticle dispersion relation $\sqrt{\mathbf{p}^2+m^2}$ with the in-medium mass m to the numerical results. We find that the dispersion relation fit remains almost constant over time during the turbulent stage of the evolution and exhibits an effective mass gap of $m \approx 0.6Q$. This plot is obtained from computations with $\lambda = 0.01$ and shown for $Qt = 1200$, but to very good accuracy, the same graph and effective mass are found for the entire range of couplings, $\lambda = 0.01 - 10$, and not too early times.

Most remarkably, our results demonstrate that the system with coupling $\lambda = 1$ still shows the same dual cascade picture as for weak couplings. From the lowest panel of Fig. 3, we see that characteristic occupation numbers for the direct energy cascade have reached $\mathcal{O}(1)$, where quantum corrections are expected to start to be become relevant. This demonstrates that, even for sizable couplings of order 1, the perturbatively expected scaling properties for the energy cascade still hold in this case. Moreover, we conclude that the nonperturbative infrared scaling properties that have been observed before from classical-statistical simulations [3,9,10] extend well beyond the weak-coupling limit.

We find for even stronger couplings important corrections to the above dual cascade picture, but the phenomenon of a significant transient increase of infrared occupancies turns out to be remarkably robust. This is demonstrated in Fig. 5(a) for the larger coupling $\lambda = 10$. One observes that for $Qt \lesssim 600$ the fluctuations in the infrared grow by more than an order of magnitude. This is much less compared to the growth of fluctuations for smaller interaction strengths, which exhibit a growth by 3 orders of magnitude in the same period of time. Remarkably, the results still suggest an approximate transient power-law behavior during this time. For later times, the infrared occupancies decrease significantly. Moreover, the occupation numbers become of order unity at the characteristic scale Q, and the distribution function approaches a Bose-Einstein distribution with vanishing chemical potential, $f_{\mathrm{BE}}(\omega) = (\mathrm{e}^{\omega/T} - 1)^{-1}$. Figure 5(b) indicates this with the dotted line representing a thermal

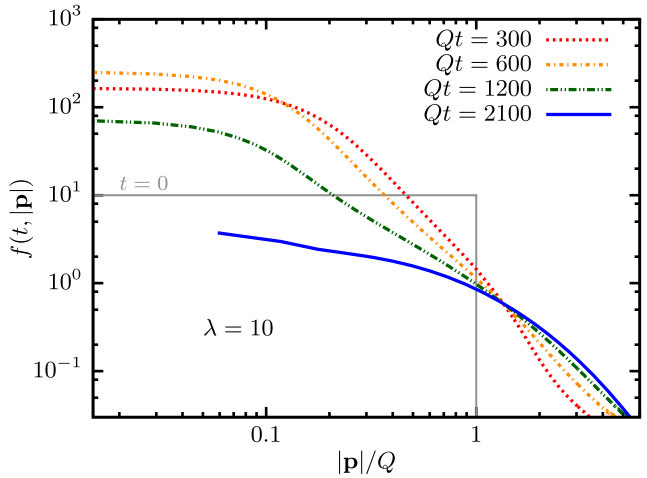

(a) Particle number distribution.

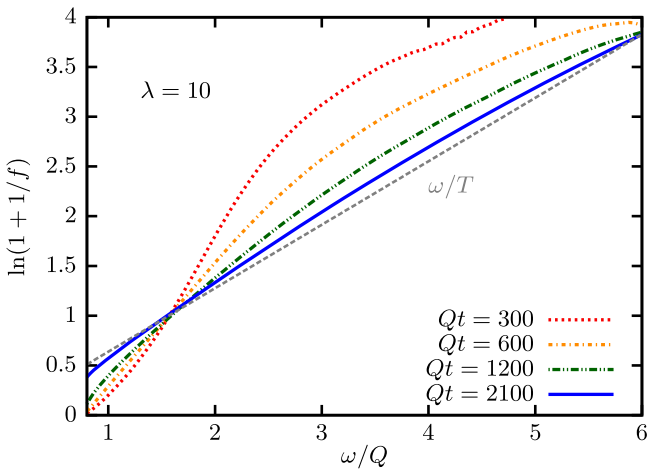

(b) Inverse slope parameter $\ln(1+1/f)$.

FIG. 5. Particle number distribution (*left*) and inverse slope parameter $\ln(1+1/f)$ (*right*) for fluctuation initial conditions with $\lambda = 10$ at different times including the initial time (solid, gray). We observe a power-law behavior for intermediate times and the approach to thermal equilibrium for $Qt \gtrsim 600$. For comparison, the dashed gray line in 5(b) corresponds to a Bose-Einstein distribution with temperature $T \approx 1.6Q$ and chemical potential $\mu = 0$.

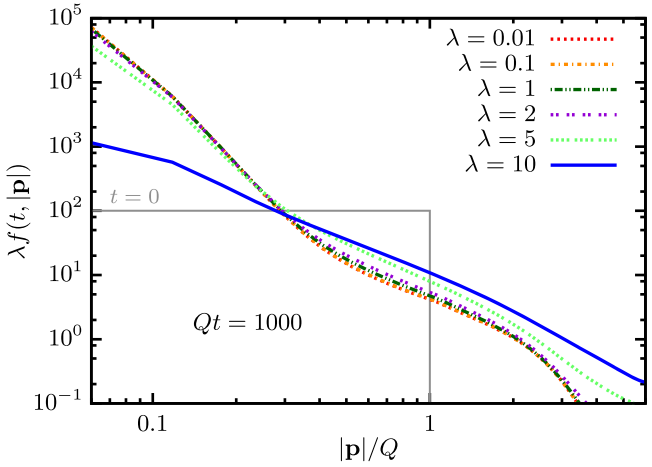

FIG. 6. Rescaled particle number distribution for fluctuation initial conditions at fixed time for different values of the coupling λ. In the range $\lambda \lesssim 2$, one observes that all curves collapse onto a single curve to good accuracy. In contrast, for stronger couplings, sizable deviations occur.

distribution with temperature $T \approx 1.6Q$. The fact that we are able to explicitly demonstrate the approach to quantum thermal equilibrium in this case has to do with the fact that it happens faster for stronger couplings, while it becomes numerically too expensive for small couplings to go to much later times.

The above observation, that even for couplings of order 1 we find transient universal scaling behavior, can be well illustrated by plotting the product $\lambda f(t, \mathbf{p})$. This product should be independent of the value of λ in the scaling regime. Figure 6 shows the quantity on spatial grids with $N_s = 135$ for $Qt = 1000$. Up to coupling constants of $\lambda \lesssim 2$, the rescaled distributions lie on top of each other to good accuracy. Differences between the rescaled distribution functions do not become sizable until the coupling has increased to about $\lambda \gtrsim 5$. This demonstrates the existence and range of attraction of the nonthermal fixed point for a wide range of couplings well beyond the weak-coupling limit.

C. Nonperturbative infrared regime

A quantity that illustrates the nonperturbative nature of the nonthermal infrared scaling regime is given by the sum of all ring diagrams entering as the main building block in the $1/N$ expansion at NLO as discussed in Sec. II and Appendix A.[4] The summation of all ring diagrams is encoded in the self-consistent equations [24]

$$I_F(t,t',\mathbf{p}) = \Pi_F(t,t',\mathbf{p}) - \int_{t_0}^{t} \mathrm{d}t'' I_\rho(t,t'',\mathbf{p})\Pi_F(t'',t',\mathbf{p}) + \int_{t_0}^{t'} \mathrm{d}t'' I_F(t,t'',\mathbf{p})\Pi_\rho(t'',t',\mathbf{p}), \tag{22}$$

$$I_\rho(t,t',\mathbf{p}) = \Pi_\rho(t,t',\mathbf{p}) - \int_{t'}^{t} \mathrm{d}t'' I_\rho(t,t'',\mathbf{p})\Pi_\rho(t'',t',\mathbf{p}), \tag{23}$$

which appear in the nonequilibrium time-evolution equations of Appendix A, with Π_F denoting the real part of the one-loop self-energy given by (11) and the corresponding imaginary part $\Pi_\rho(t,t',\mathbf{p}) = F_{ab}(t,t',\mathbf{p})\rho_{ab}(t,t',\mathbf{p})/(3N)$. By iteration, the above equations can be seen to generate the ring diagrams, which are contained in I_F and I_ρ, to infinite loop order. It is instructive to compare the one-loop self-energy $\Pi_F(t,t,\mathbf{p})$ at equal times to the one including all NLO large-N corrections as given by $I_F(t,t,\mathbf{p})$. More precisely, we consider the ratio

$$\frac{I_F(t,t,\mathbf{p})}{\Pi_F(t,t,\mathbf{p})} = 1 - \frac{\int_{t_0}^{t} \mathrm{d}t''(I_\rho\Pi_F - I_F\Pi_\rho)}{\Pi_F(t,t,\mathbf{p})}, \tag{24}$$

where the rhs follows from (22) evaluated at equal times, $t = t'$. In a perturbative regime, we expect I_F to be dominated by the lowest one-loop contribution Π_F such that the ratio (24) is about 1.

From the top panel of Fig. 7 for $\lambda = 0.01$, one observes that the ratio (24) decreases over several orders of magnitude in the low momentum regime during those times where the transient inverse particle cascade occurs according to the results of Sec. III B. Around the inflection point of the I_F/Π_F curve on a double logarithmic scale, we find an approximate slope corresponding to a drop in momenta $\sim|\mathbf{p}|^{3.4}$ at $Qt = 1200$. At large momenta, the ratio approaches unity as anticipated but still differs sizably from 1 in the momentum range of the energy cascade.

We have verified that the values found for $\lambda = 0.1$ agree well with those obtained for $\lambda = 0.01$, which holds to good accuracy even for $\lambda = 1$ as demonstrated with the middle panel of Fig. 7. For $\lambda = 10$, the bottom panel of Fig. 7 shows significant deviations from unity in the infrared at intermediate times, while the ratio approaches unity again for later times where the $\lambda = 10$ results already thermalize. This reflects the fact that occupation numbers first increase for small momenta as a consequence of the inverse particle cascade and then approach order unity on their way to thermal equilibrium.

D. Classical-statistical field theory limit

As discussed in Sec. II (cf. also Appendix A), we can study the corresponding classical-statistical field theory in the same framework of the $1/N$ expansion to NLO following along the lines of Ref. [13]. In Ref. [3], the

[4]The relation of the ring sum at NLO in the large-N expansion to an effective vertex resummation is explained in Refs. [10,25,32].

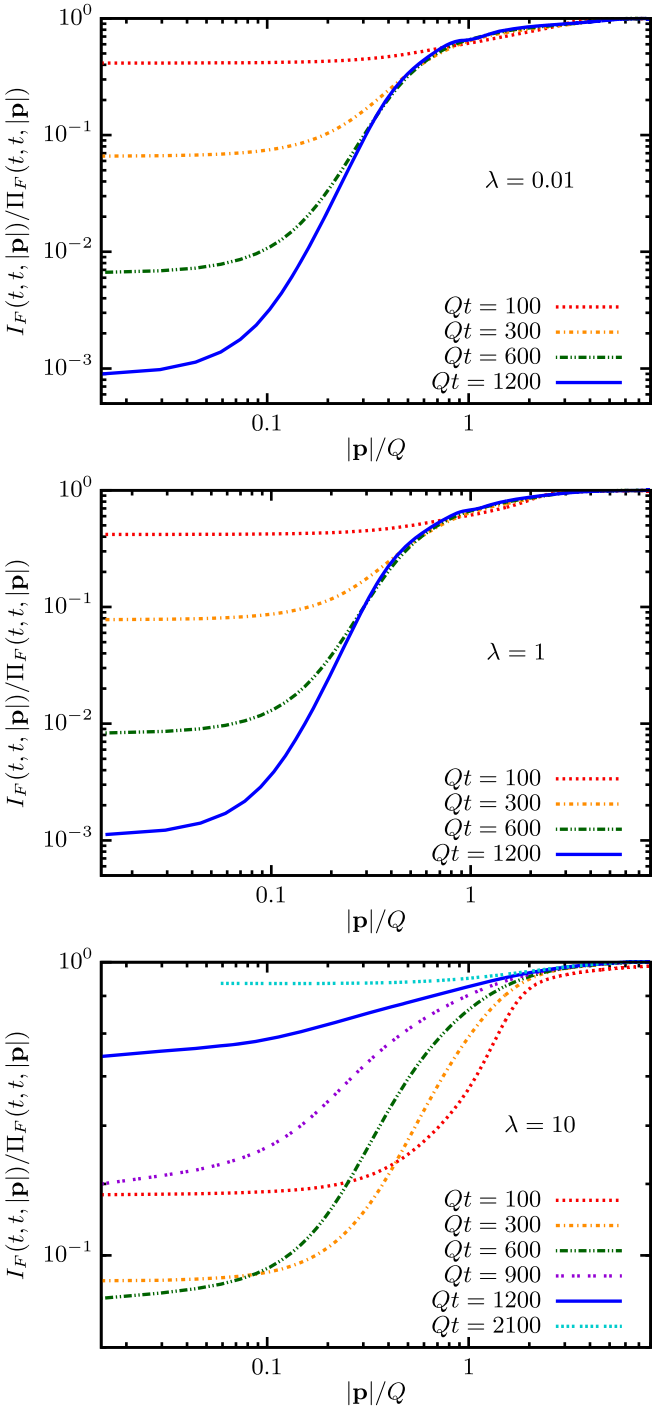

FIG. 7. The ratio (24) for fluctuation initial conditions with $\lambda = 0.01, 1, 10$ (*top* to *bottom*). In a perturbative regime, I_F is expected to be dominated by the lowest one-loop contribution Π_F such that the ratio (24) is about 1. While at high momenta the ratio approaches unity, in the infrared regime, one observes very strong deviations from 1 for times where the transient inverse particle cascade occurs.

agreement of the quantum dynamics with results from classical-statistical simulations during parametric resonance at early times for the same model was shown to agree well for weak couplings. A similar study [33], employing the tachyonic instability, also reports a matching of both methods.

The range of validity of the classical-statistical approach was also studied extensively in Ref. [19] for a massless one-component scalar field theory. In particular, Ref. [19] reported that if the classical-statistical evolutions are started from quantum initial conditions, the subsequent dynamics can lead to the decay of the initial quantum-half if the couplings are too strong. Here, we add to these findings by a direct comparison between the quantum and classical evolutions, i.e. by solving the evolution equations at NLO in the $1/N$ expansion both for the classical-statistical theory and for the quantum theory starting from the same fluctuation initial conditions.

Figure 8 shows our results for $\lambda = 10$ at time $Qt = 1000$ for the quantum (dashed line) and the classical (solid line) evolution. At this time, we find that the sum $f(t,|\mathbf{p}|) + 1/2$ as obtained from the classical evolution can already be described by a classical thermal distribution $T/(\omega - \mu)$ with temperature T, dispersion relation $\omega = \sqrt{\mathbf{p}^2 + m^2}$, and chemical potential μ. Since the classical thermal distribution leads to the Rayleigh-Jeans divergence, all classical thermal results depend on the employed ultraviolet cutoff $\Lambda_{\rm UV} = 7.9Q$. For this cutoff, we find $T \approx 6.7Q$ and $\mu \approx -6.5Q$ at $Qt = 1000$ with an in-medium mass $m \approx 0.7Q$, where the latter was obtained from the numerically computed dispersion relation as in Sec. III B.

By comparison to the horizontal line in Fig. 8, we see that for the classical evolution the sum $f(t,|\mathbf{p}|) + 1/2$ drops below $1/2$ for high momenta. This shows the decay of the initial vacuum quantum-half and, hence, is outside the range

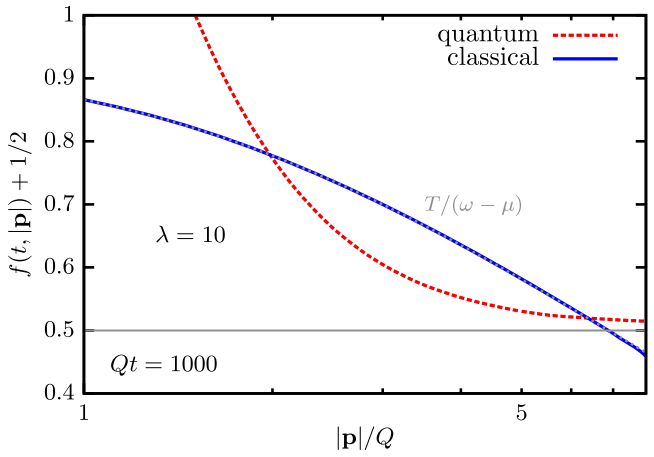

FIG. 8. The sum $f(t,|\mathbf{p}|) + 1/2$ for $\lambda = 10$ at time $Qt = 1000$ for the quantum (dashed line) and the classical (solid line) evolution for fluctuation initial conditions. In addition, we show the classical thermal function $T/(\omega(\mathbf{p}) - \mu)$ (gray, dotted) for comparison, with parameters as described in the main text. One observes that, in contrast to the quantum evolution, the classical results for $f(t,|\mathbf{p}|) + 1/2$ drop below $1/2$ at high momenta, showing the decay of the initial quantum-half.

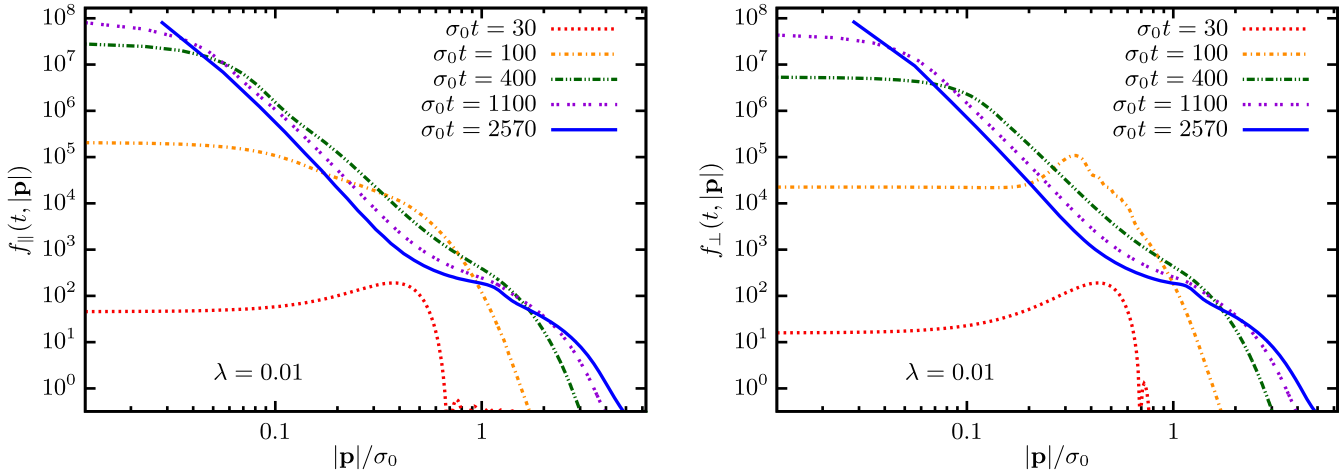

FIG. 9. Longitudinal (∥, *left*) and transverse (⊥, *right*) occupation number distributions for macroscopic field initial conditions with $\lambda = 0.01$ at different times showing the emergence of a dual cascade picture.

of validity of the classical-statistical approximation to describe the quantum dynamics in this case. In contrast, in the quantum theory, $f(t, |\mathbf{p}|)$ never reaches negative values and is seen to approach a Bose-Einstein distribution at late times. Of course, classical dynamics cannot describe the approach to quantum thermal equilibrium, and for given finite coupling and ultraviolet regularization, the classical description is only valid for a restricted time. The smaller the coupling, the later the breakdown of the classical-statistical approximation occurs, which is also what we observe.[5]

IV. RESULTS STARTING FROM MACROSCOPIC FIELD INITIAL CONDITIONS

A. Nonthermal fixed points

In addition to the fluctuation initial conditions with vanishing macroscopic field discussed in the previous section, we also investigate the time evolution starting from a macroscopic field with only vacuum fluctuations as described in Sec. II B. We can see from Fig. 9 for $\lambda = 0.01$ that the system builds up highly occupied modes in the infrared very quickly through the mechanism of parametric resonance with the initial characteristic resonance peak at $|\mathbf{p}| \sim \sigma_0/\sqrt{2}$ [29]. One observes that the early-time evolution of the longitudinal and transverse degrees of freedom differs, but they become almost indistinguishable from each other at later times. This is due to the fact that the macroscopic field decays with time.

Similar to what is found for fluctuation initial conditions, the inverse particle cascade in the infrared can be clearly observed from Fig. 9. A fit produces a value of $\kappa_N \approx 4.7$ for the associated stationary exponent at the available times, which is expected to increase further for later times. The dispersion relation of this system is approximately constant in the momentum range of the particle cascade, very similar to the relation obtained from the fluctuation initial conditions (cf. Fig. 4). Fitting a power law $\sim|\mathbf{p}|^{-3/2}$ at higher momenta hints to a direct energy cascade [31], but the resonance peaks have not yet smoothed out at the latest times we consider.

The computations with an interaction strength of $\lambda = 0.1$ yield practically the same distributions as just discussed for $\lambda = 0.01$ up to a rescaling with the coupling as expected from the discussion for the symmetric case above. When increasing the coupling to $\lambda = 1$, the overall picture as presented in Fig. 10 remains very similar if compared to the weak-coupling results displayed in Fig. 9. We find that the particle cascade at low momenta can be fitted with power laws $\sim|\mathbf{p}|^{-4.6}$ and $\sim|\mathbf{p}|^{-4.8}$ for longitudinal and transverse modes, respectively. We note that they still increase to larger values over time.

A significantly modified picture emerges for the distribution functions for a coupling of $\lambda = 10$, which we show in Fig. 11 for both longitudinal and transverse modes. We

[5]In general, for a self-interacting boson field φ with coupling λ, the mapping between the quantum and the classical description involves two steps [1,12]: first, one separates the quantum field $\varphi = \phi + \delta\varphi$ into a (large) coherent part with expectation value $\langle\varphi\rangle = \phi \sim Q/\sqrt{\lambda}$ and a (small) fluctuation with $\langle\delta\varphi^2\rangle \sim Q^2$ for some given momentum scale Q and coupling parameter $\lambda \ll 1$. The early-time dynamics can then be linearized in the fluctuations as long as $\langle\delta\varphi^2\rangle \ll Q^2/\lambda$ and solved. Albeit small initially, the fluctuations can grow with time because of nonequilibrium instabilities. Once the fluctuations become larger, one uses the outcome of the linearized early-time evolution as input for a subsequent fully nonlinear classical-statistical simulation. The whole procedure has a well-defined continuum limit for sufficiently weak couplings (see also Ref. [34]). Instead of this two-step procedure, a simplified description is often employed: the fully nonlinear classical-statistical simulation is considered right from the beginning as a shortcut procedure. In this case, for strong-field initial conditions, the description is only valid as a low-energy effective theory for a finite time depending on the employed coupling and ultraviolet cutoff scale [35].

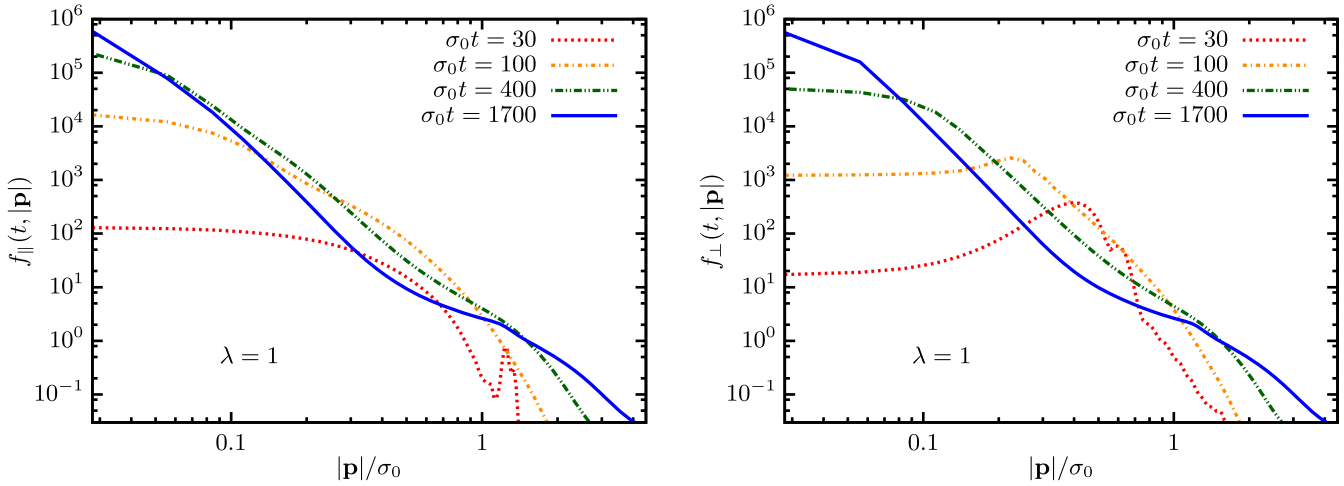

FIG. 10. As in Fig. 9, but for $\lambda = 1$, for which the system is still showing a dual cascade picture.

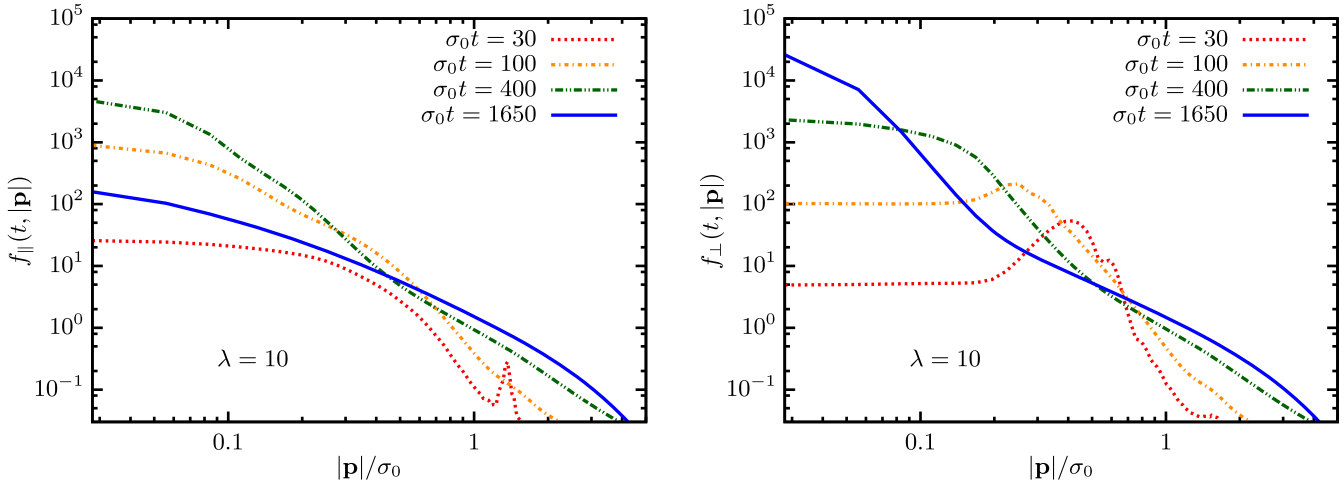

FIG. 11. As in Fig. 9, but for $\lambda = 10$, where strong deviations from the dual cascade picture occur. The longitudinal spectrum approaches thermal equilibrium rather quickly. At the same time, the transverse occupation number distribution exhibits a cascadelike behavior for small momenta, while the ultraviolet already shows signs of thermalization.

observe an increase of the longitudinal occupation number in the infrared for $\sigma_0 t \lesssim 400$, with a subsequent decrease at later times. For large momenta, a quick approach to a thermal-like curve is observed, which is reminiscent of the situation described in Sec. III B for fluctuation initial conditions. At the same time, the transverse modes still exhibit a cascadelike behavior in the infrared, as can be seen from the evolution for times $\sigma_0 t \gtrsim 200$. Part of the curve in the infrared could be fitted with a power law $\sim |\mathbf{p}|^{-4.5}$ at $\sigma_0 t = 1650$. Both the scaling exponent and the distribution function in the deep infrared still grow at the latest time available and are far from equilibrium. Whereas the ultraviolet appears closer to thermal equilibrium for both the longitudinal and transverse degrees of freedom (they are approximately equal for $|\mathbf{p}| \gtrsim 0.3\sigma_0$ at the latest time shown), they differ in the infrared by more than 2 orders of magnitude at $\sigma_0 t = 1650$.

In Fig. 12, where the inverse slope parameter for both the longitudinal and transverse degrees of freedom is presented, we can explicitly see the approach to a Bose-Einstein distribution with temperature $T \approx \sigma_0$ and chemical potential $\mu \approx 0.7\sigma_0$ at the latest available time ($\sigma_0 t = 1650$). For the real scalar field theory, we expect this distribution to still evolve until a vanishing chemical potential is reached [24]. Moreover, the fast isotropization in field space is apparent as the curves are very similar for $\sigma_0 t = 100$ and already indistinguishable for $\sigma_0 t = 400$.

Finally, we present the rescaled distribution functions $\lambda f_{\parallel,\perp}(t, \mathbf{p})$ for fixed times in the symmetry-broken regime in Fig. 13, which are obtained through calculations where spatial grids with $N_s = 128$, $\sigma_0 a_s = 1.0$ and a temporal step size $\sigma_0 a_t = 0.2$ are used. The rescaled spectra lie on top of each other to good accuracy well beyond the weak-coupling regime up to $\lambda \lesssim 2$. The deviations start to occur

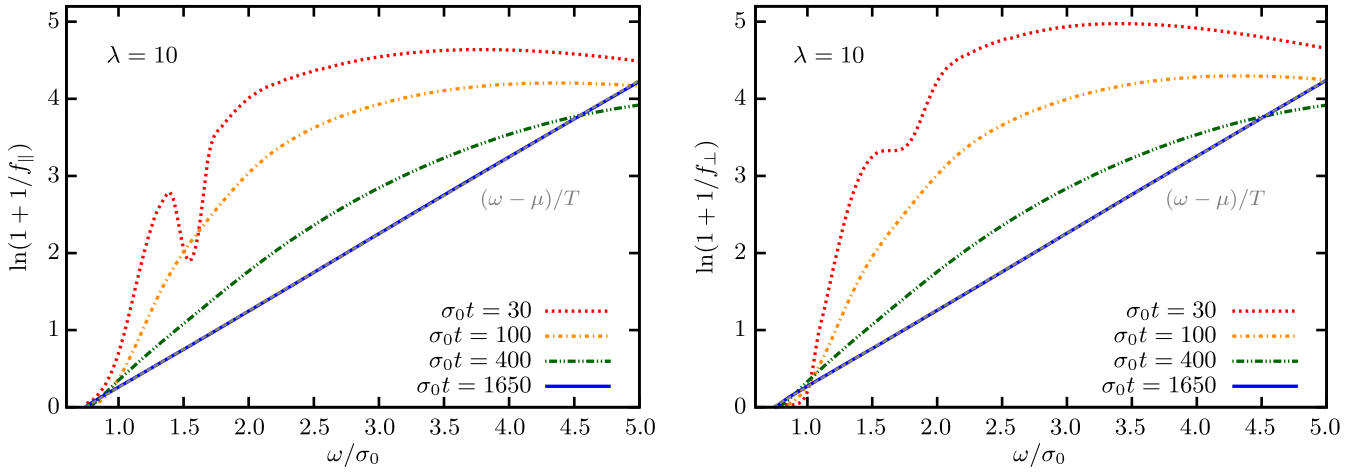

FIG. 12. Longitudinal (∥, *left*) and transverse (⊥, *right*) inverse slope parameters $\ln(1 + 1/f_{\parallel,\perp})$ for macroscopic field initial conditions with $\lambda = 10$ at different times. We observe the approach to thermal equilibrium. For comparison, the dashed line in each plot corresponds to a Bose-Einstein distribution with temperature $T \approx \sigma_0$ and chemical potential $\mu \approx 0.7\sigma_0$.

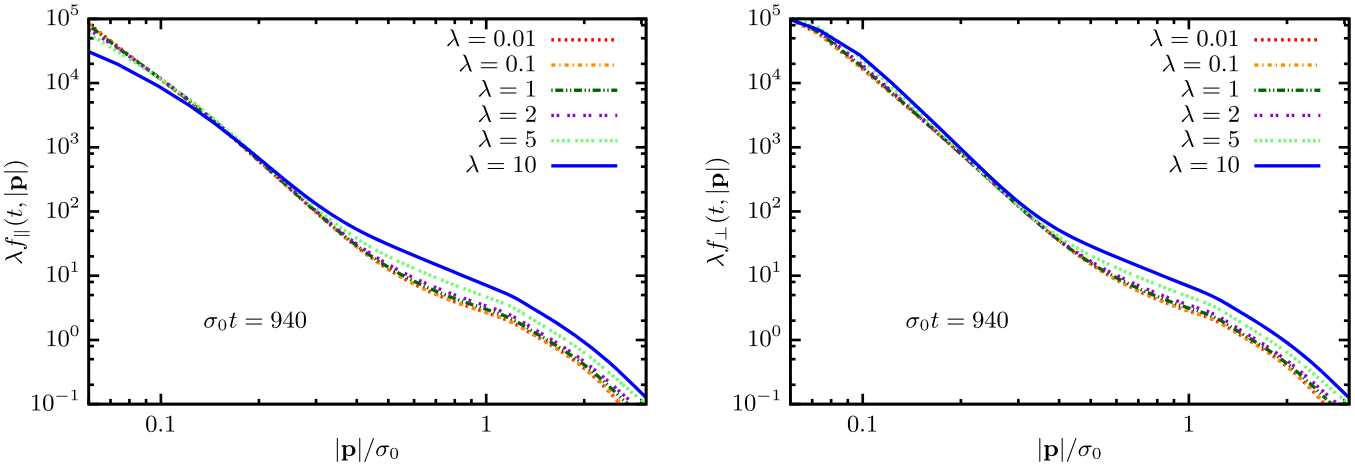

FIG. 13. Rescaled longitudinal (∥, *left*) and transverse (⊥, *right*) occupation number distributions for macroscopic field initial conditions at fixed time $\sigma_0 t = 940$ for different values of the coupling λ.

first in the energy cascade, whereas the particle cascade still exhibits good agreement. In the latter momentum range, differences between the rescaled distribution functions do not become sizable until the coupling has increased to $\lambda > 5$. Moreover, the deviations for the transverse low-momentum modes are smaller if compared to the ones for the longitudinal direction, whereas they agree well for larger momenta.

B. Macroscopic field dynamics

In the following, we investigate the time evolution of the macroscopic field $\phi(t)$. Figure 14 shows the time evolution of the envelope of the macroscopic field amplitude, $\phi_{\max}$. The macroscopic field itself oscillates rapidly as can be inferred from the inset of the figure. The oscillation frequency retains its value over the computed period of time and is set by the same dynamically generated effective mass, $\omega_\phi \approx 0.7\sigma_0$, as inferred from the dispersion relation which has the same form as in the symmetric regime, cf. Fig. 4.

After the end of parametric resonance, there is an intermediate power-law decay of the field amplitude $\sim t^{-c}$ with $c \approx 0.5$. Comparing to the evolution of the distribution function, we observe that this decay happens during the approach to the self-similar turbulent regime. At about $\sigma_0 t \approx 200$, the field decay slows down, and the amplitude may be described by a power law with a much smaller exponent. Moreover, the isotropization of the system in field space can be attributed to the decay of the macroscopic field as it becomes less important and leads to a decrease in the difference between the longitudinal and transverse degrees of freedom.

Going beyond the weakly coupled regime, we present the dynamics of the macroscopic field for $\lambda = 1$ and 10 in Figs. 15 and 16, respectively. Overall, the oscillation

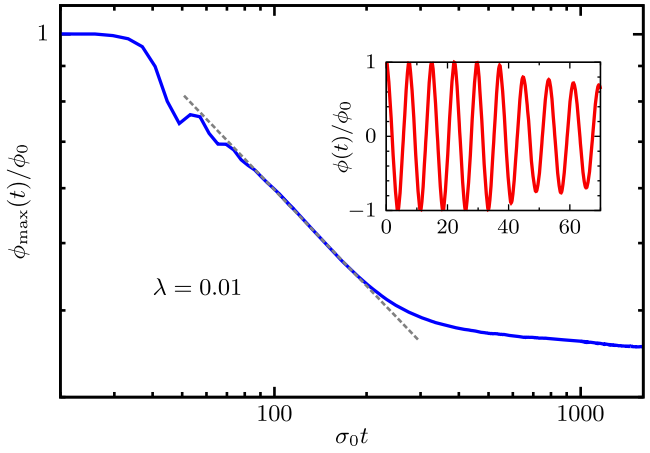

FIG. 14. Double-logarithmic plot of the time evolution of the envelope $\phi_{\max}(t)$ normalized to its initial value ϕ_0 for $\lambda = 0.01$. In the inset, the oscillating field is displayed. The field amplitude is $\sim t^{-c}$ with $c \approx 0.5$ at intermediate times and with a much smaller exponent of the order of a few percent during the turbulent stages of the evolution at later times.

frequency and, therefore, the effective mass again remain approximately constant during the evolution. For intermediate times, i.e. after the end of the instability and during the approach to the turbulent stage of the evolution, we observe an intermediate power law $\sim t^{-c}$ with $c \approx 0.4$ for the smaller coupling displayed, $\lambda = 1$. Later on, the maximum field amplitude follows a very slow exponential decay in contrast to the weak power-law behavior found in the weakly coupled regime. In the case of the stronger coupling of $\lambda = 10$, the field oscillations are exponentially damped with a rate of about $\sim 10^{-3}\sigma_0$, which results in an almost vanishing field expectation value for the latest times shown.

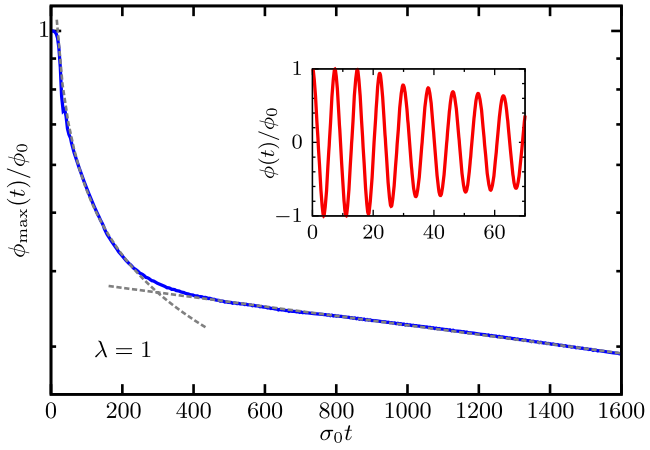

FIG. 15. For $\lambda = 1$, the power law of the field amplitude $\phi_{\max}(t)$ is $\sim t^{-c}$ with $c \approx 0.4$ for intermediate times (note the log-lin plot). At later times, an exponential damping with a small rate $\sim 10^{-4}\sigma_0$ is found.

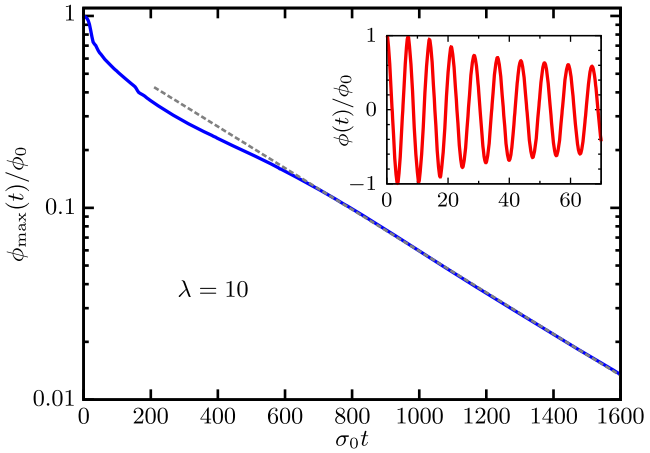

FIG. 16. For $\lambda = 10$, we observe an exponential decay of the field amplitude $\phi_{\max}(t)$ with a rate of about $\sim 10^{-3}\sigma_0$ (dashed line).

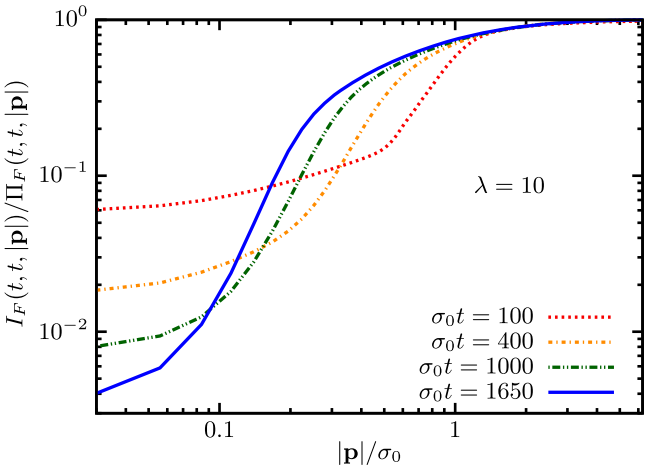

FIG. 17. The ratio (24) for macroscopic field initial conditions with $\lambda = 10$ for different times.

C. Nonperturbative infrared regime

As for the fluctuation initial conditions, we also investigate the ratio (24) in the symmetry-broken regime. We find the same behavior as discussed for the symmetric regime in Sec. III C for interaction strengths in the range $\lambda = 0.01 - 1$. This agreement corresponds to the fact that one observes very similar results from the numerical calculations with both initial conditions in the low-momentum regime in Secs. III B and IV A (cf. Figs. 3, 9, and 10). For $\lambda = 10$, the ratio is displayed in Fig. 17. In view of our findings for fluctuation initial conditions, it exhibits still a remarkably similar behavior to the one observed for weaker couplings.

V. SUMMARY AND CONCLUSIONS

For the example of a self-interacting N-component scalar quantum field theory in a large-N expansion to next-to-leading order, we have shown that nonthermal fixed points

are approached from large-field or overoccupied initial conditions. Remarkably, we find the associated transient universal scaling behavior also beyond the weak-coupling limit, well beyond the range of validity of classical-statistical simulations. This concerns in particular the presence of an inverse particle cascade with very large occupancies in the infrared, the characteristic properties of which can be found for couplings as large as $\lambda \sim \mathcal{O}(10)$. While these results may be unexpected in view of genuine weak-coupling techniques such as the classical-statistical approach or quantum kinetic theory, we emphasize that corresponding findings of universal behavior being insensitive to the values of couplings are well known for the (albeit different) case of scaling behavior near phase transitions in thermal equilibrium.

The central results of this paper can all be seen in the bottom panel of Fig. 3, which displays the evolution of the distribution function at $\lambda = 1$ starting from overoccupied initial conditions. It demonstrates the turbulent dual cascade picture, with an inverse particle cascade and a direct energy cascade, directly in quantum field theory and beyond the weak-coupling limit. Moreover, it shows the emergence of the expected perturbative scaling exponent $\kappa_{\mathrm{E}} = 5/3$ associated with the direct energy cascade at large momenta for vanishing macroscopic field. It also reflects the fact that at small momenta the dynamics becomes nonrelativistic with a nonperturbative stationary exponent of $\kappa_{\mathrm{N}} = 5$.

In addition, we analyzed the role and importance of the quantum corrections to stabilize the quantum vacuum beyond the weak-coupling limit and presented a detailed comparison to the dynamics starting from strong-field initial conditions. In scenarios including a macroscopic field for the coupling parameter $\lambda = 10$, we discovered a hybrid picture of turbulent behavior reminiscent of the particle cascade in the infrared and an approach toward thermal equilibrium in the ultraviolet for the transverse modes, while the longitudinal degrees of freedom approach quantum thermal equilibrium in the entire momentum range.

Our findings challenge perturbative kinetic descriptions of thermalization dynamics starting from strong-field or overoccupied initial conditions. This has to be seen also in view of the findings of Ref. [23], where disagreements between classical-statistical simulations and kinetic theory even in the weak-coupling regime were observed, and where the origin of the discrepancies can be traced back to the emergence of nonperturbatively large occupancies in the infrared. In turn, the successful application of the NLO large-N summation in describing this physics may be used as a starting point for improved kinetic descriptions [10].

The nonrelativistic behavior in the infrared allows also direct comparisons to the dynamics of ultracold quantum gas systems out of equilibrium [9]. Based on the universality observed between highly occupied scalar and gauge field dynamics at weak couplings in Ref. [11], our results may also be helpful in understanding the dynamics of aspects of gauge theories far from equilibrium beyond the weak-coupling limit relevant for relativistic heavy-ion collisions. For further investigations related to cosmological inflation, it should be considered to extend the computations including fermions [36,37] to isotropically expanding space-times for more realistic models, which has been started in Refs. [38,39] for de Sitter space.

ACKNOWLEDGMENTS

We would like to thank Kirill Boguslavski, Daniil Gelfand, Valentin Kasper, Asier Piñeiro Orioli, Alexander Rothkopf, Sören Schlichting, and Raju Venugopalan for discussions/collaboration on related work. B. W. gratefully acknowledges support from the Studienstiftung des deutschen Volkes, a Starting Grant of the European Research Council (Grant No. 279617), a Cambridge European Scholarship of the Cambridge Trust, and a Science and Technology Facilities Council (STFC) Studentship. Parts of this work were performed on the computational resource bwUniCluster funded by the Ministry of Science, Research and the Arts Baden-Württemberg and the Universities of the State of Baden-Württemberg, Germany, within the framework program bwHPC. This work is part of and supported by the Deutsche Forschungsgemeinschaft (DFG) Collaborative Research Centre "SFB 1225 (ISOQUANT)."

APPENDIX A: NLO EVOLUTION EQUATIONS

In this Appendix, we review the nonequilibrium evolution equations from the large-N expansion to NLO of the 2PI effective action and refer to the literature for their derivation [24,25]. Starting from the Gaussian initial conditions of Sec. II B, the evolution equations for the quantum-statistical anticommutator F defined in (7) and commutator ρ defined in (9) are

$$[\Box_x \delta_{ac} + M^2_{ac}(x)] F_{cb}(x,y) = -\int_{t_0}^{x^0} \mathrm{d}z\, \Sigma^{\rho}_{ac}(x,z) F_{cb}(z,y) + \int_{t_0}^{y^0} \mathrm{d}z\, \Sigma^{F}_{ac}(x,z) \rho_{cb}(z,y), \tag{A1}$$

$$[\Box_x \delta_{ac} + M^2_{ac}(x)] \rho_{cb}(x,y) = -\int_{y^0}^{x^0} \mathrm{d}z\, \Sigma^{\rho}_{ac}(x,z) \rho_{cb}(z,y) \tag{A2}$$

with shorthand notation $\int_{t_1}^{t_2} \mathrm{d}z \equiv \int_{t_1}^{t_2} \mathrm{d}z^0 \int \mathrm{d}^3 z$ and initial time t_0.

For a quantum theory with classical Lagrangian (1) and field rescaling (3), the space-time-dependent effective mass term $M^2_{ab}(x)$ is given by

$$M^2_{ab}(x;\phi,F) = \frac{1}{6N}[F_{cc}(x,x) + \phi^2(x)]\delta_{ab} + \frac{1}{3N}[F_{ab}(x,x) + \phi_a(x)\phi_b(x)]. \tag{A3}$$

The real and imaginary parts of the self-energy, $\Sigma^F_{ac}(x,y)$ and $\Sigma^\rho_{ac}(x,y)$, are at NLO:

$$\Sigma^F_{ab}(x,y) = -\frac{1}{3N}\Big\{ I_F(x,y)\phi_a(x)\phi_b(y) + [I_F(x,y)+P_F(x,y)]F_{ab}(x,y) - \left(\frac{\lambda}{2}\right)^2 [I_\rho(x,y)+P_\rho(x,y)]\rho_{ab}(x,y)\Big\}, \quad \text{(A4)}$$

$$\Sigma^\rho_{ab}(x,y) = -\frac{1}{3N}\{ I_\rho(x,y)\phi_a(x)\phi_b(y) + [I_\rho(x,y)+P_\rho(x,y)]F_{ab}(x,y) + [I_F(x,y)+P_F(x,y)]\rho_{ab}(x,y)\}. \quad \text{(A5)}$$

Here, the ϕ-independent summation functions I_F and I_ρ are defined by

$$I_F(x,y) = \Pi_F(x,y) - \int_{t_0}^{x^0} \mathrm{d}z\, I_\rho(x,z)\Pi_F(z,y) + \int_{t_0}^{y^0} \mathrm{d}z\, I_F(x,z)\Pi_\rho(z,y), \quad \text{(A6)}$$

$$I_\rho(x,y) = \Pi_\rho(x,y) - \int_{y^0}^{x^0} \mathrm{d}z\, I_\rho(x,z)\Pi_\rho(z,y), \quad \text{(A7)}$$

where we used $\Pi_F(x,y;F,\rho) = [F_{ab}(x,y)F_{ab}(x,y) - (\lambda/2)^2\rho_{ab}(x,y)\rho_{ab}(x,y)]/(6N)$ as well as $\Pi_\rho(x,y;F,\rho) = [F_{ab}(x,y)\rho_{ab}(x,y)]/(3N)$ as defined in Secs. II A and III C. The ϕ-dependent summation functions P_F and P_ρ, which vanish in the symmetric regime ($\phi = 0$), are given by

$$P_F(x,y) = J_F(x,y) - \int_{t_0}^{x^0} \mathrm{d}z\, I_\rho(x,z)J_F(z,y) + \int_{t_0}^{y^0} \mathrm{d}z\, I_F(x,z)J_\rho(z,y), \quad \text{(A8)}$$

$$P_\rho(x,y) = J_\rho(x,y) - \int_{y^0}^{x^0} \mathrm{d}z\, I_\rho(x,z)J_\rho(z,y), \quad \text{(A9)}$$

where we defined

$$J_F(x,y) = H_F(x,y) - \int_{t_0}^{x^0} \mathrm{d}z\, H_\rho(x,z)I_F(z,y) + \int_{t_0}^{y^0} \mathrm{d}z\, H_F(x,z)I_\rho(z,y), \quad \text{(A10)}$$

$$J_\rho(x,y) = H_\rho(x,y) - \int_{y^0}^{x^0} \mathrm{d}z\, H_\rho(x,z)I_\rho(z,y) \quad \text{(A11)}$$

with $H_F(x,y) = \phi_a(x)F_{ab}(x,y)\phi_b(y)/(3N)$ and $H_\rho(x,y) = \phi_a(x)\rho_{ab}(x,y)\phi_b(y)/(3N)$. With these definitions, one observes that $I_{F,\rho}$, $P_{F,\rho}$, and $J_{F,\rho}$ have the same form. Finally, the evolution equation for the macroscopic field at NLO can also be given in terms of these quantities:

$$\left\{\left[\Box_x + \frac{1}{6N}\phi^2(x)\right]\delta_{ab} + M^2_{ab}(x)|_{\phi=0}\right\}\phi_b(x) = -\int_{t_0}^{x^0} \mathrm{d}y\, \Sigma^\rho_{ac}(x,y)|_{\phi=0}\phi_b(y). \quad \text{(A12)}$$

To conclude this Appendix, we note that the classical-statistical field theory limit corresponds to neglecting the quantum-half in the above evolution equations, i.e. putting everywhere $\lambda/2$ to zero taking into account the field rescaling (3). There are no other changes concerning the form of the evolution equations; however, in the classical theory, the field two-point correlator plays the role of the anticommutator expectation value of the quantum theory, and the Poisson bracket replaces the commutator expectation value [13,40].

APPENDIX B: MASS RENORMALIZATION

It turns out that it is sufficient for the employed parameter ranges to consider a mass renormalization which cancels the quadratically divergent mass terms at initial time for a cutoff-regularized theory. We explicitly checked that the renormalization procedure, which we describe in the following, leads to cutoff-insensitive results for the accessible grid sizes. Renormalization of initial-value problems is further discussed in Ref. [41]. We calculate the mass counterterms of the Gaussian theory at initial time iteratively. Because the macroscopic field initial conditions break the O(N) symmetry, the dressings of the longitudinal and transverse degrees of freedom differ, and we consider them separately in that case.

For vanishing renormalized vacuum mass, we determine the initial renormalized in-medium mass $M_{0,\parallel/\perp}(\phi,F)$ by self-consistently solving the mass gap equations involving the macroscopic field and the tadpole contribution,

$$M^2_{0,\parallel}(\phi,F) = \frac{1}{6N}\left[3\int_{\mathbf{p}}^{\Lambda} F_\parallel(0,0,|\mathbf{p}|) + 3\phi^2(0) + (N-1)\int_{\mathbf{p}}^{\Lambda} F_\perp(0,0,|\mathbf{p}|)\right] + \delta m^2_\parallel, \quad \text{(B1)}$$

$$M^2_{0,\perp}(\phi,F) = \frac{1}{6N}\left[\int_{\mathbf{p}}^{\Lambda} F_\parallel(0,0,|\mathbf{p}|) + \phi^2(0) + (N+1)\int_{\mathbf{p}}^{\Lambda} F_\perp(0,0,|\mathbf{p}|)\right] + \delta m^2_\perp, \quad \text{(B2)}$$

where we used the shorthand notation $\int_{\mathbf{p}}^{\Lambda} \equiv \int^{\Lambda} \frac{\mathrm{d}^3p}{(2\pi)^3}$. Here, the initial statistical propagators depend on the effective mass as well, cf. Eq. (13). We choose to cancel the leading quadratic cutoff dependence of the three-dimensional momentum integrals over the initial statistical propagators by the counterterms $\delta m^2_\parallel$ and $\delta m^2_\perp$, which are given by

$$\delta m_{\parallel}^2 = -\frac{1}{6N}\left[\frac{3}{2}\int_{\mathbf{p}}^{\Lambda}(\mathbf{p}^2+M_{0,\parallel}^2)^{-1/2} + \frac{(N-1)}{2}\int_{\mathbf{p}}^{\Lambda}(\mathbf{p}^2+M_{0,\perp}^2)^{-1/2}\right], \quad \text{(B3)}$$

$$\delta m_{\perp}^2 = -\frac{1}{6N}\left[\frac{1}{2}\int_{\mathbf{p}}^{\Lambda}(\mathbf{p}^2+M_{0,\parallel}^2)^{-1/2} + \frac{(N+1)}{2}\int_{\mathbf{p}}^{\Lambda}(\mathbf{p}^2+M_{0,\perp}^2)^{-1/2}\right]. \quad \text{(B4)}$$

During the initialization procedure these equations are iteratively solved starting with $M_{0,\parallel}^2 = M_{0,\perp}^2 = 0$ until convergence is achieved. The same counterterms are employed to also cancel the associated divergences in the equations of motion.

APPENDIX C: ENERGY-MOMENTUM TENSOR

Since the energy density is a conserved quantity, we can use it to check the numerical accuracy of our calculations and find very good stability. We obtain this quantity as the T^{00}-component of the energy-momentum tensor $T^{\mu\nu}$ and consider spatially homogeneous and isotropic systems. It is useful to split the energy density $\epsilon = \lim_{V\to\infty}(T^{00}/V)$ in its classical and fluctuation parts,

$$\epsilon = \epsilon_{\rm class}(t) + \epsilon_{\rm fluc}(t). \quad \text{(C1)}$$

The former only depends on the macroscopic field and can be easily calculated from the action. For the massless theory, taking into account the field rescaling (3), we get

$$\lambda\epsilon_{\rm class}(t) = \frac{1}{2}\dot{\phi}^2(t) + \frac{1}{4!N}\phi^4(t), \quad \text{(C2)}$$

where we omitted the spatial derivatives as we assume spatial homogeneity. In the symmetric regime, this quantity vanishes identically.

Employing the $1/N$ expansion of the 2PI effective action at NLO for a cutoff-regularized theory, we obtain for the fluctuation part of the energy density with all quantities given in Fourier space:

$$\lambda\epsilon_{\rm fluc}(t) = \frac{1}{2}\int_{\mathbf{p}}[\partial_t\partial_{t'}F_{aa}(t,t';|\mathbf{p}|)|_{t=t'} + \mathbf{p}^2F_{aa}(t,t;|\mathbf{p}|) + M_{ab}^2(t)|_{F=0}F_{ab}(t,t;|\mathbf{p}|)] + \frac{1}{4!N}\left(\int_{\mathbf{p}}F_{aa}(t,t;|\mathbf{p}|)\right)^2 + \frac{1}{2}\int_{\mathbf{p}}I_F(t,t;|\mathbf{p}|) + \int_{\mathbf{p}}\left[\frac{1}{2}P_F(t,t;|\mathbf{p}|) - \frac{1}{6N}H_F(t,t;|\mathbf{p}|)\right], \quad \text{(C3)}$$

where summation over repeated indices is implied. The effective mass term M_{ab}^2 is provided in (A3), whereas the real-space summation functions I_F and P_F can be found in (A6) and (A8), respectively. Under the stated assumptions, we additionally have $H_F(t,t';|\mathbf{p}|) = \phi_a(t)F_{ab}(t,t',|\mathbf{p}|)\phi_b(t')$. Finally, the last integral in (C3) is absent in the symmetric regime, and we point out that the energy density does not contain the spectral function as it vanishes at equal times due to the bosonic commutation relations.

[1] S. Khlebnikov and I. Tkachev, Classical Decay of the Inflaton, Phys. Rev. Lett. **77**, 219 (1996).
[2] R. Micha and I. Tkachev, Relativistic Turbulence: A Long Way from Preheating to Equilibrium, Phys. Rev. Lett. **90**, 121301 (2003).
[3] J. Berges, A. Rothkopf, and J. Schmidt, Nonthermal Fixed Points: Effective Weak Coupling for Strongly Correlated Systems Far from Equilibrium, Phys. Rev. Lett. **101**, 041603 (2008).
[4] T. Lappi and L. McLerran, Some features of the glasma, Nucl. Phys. **A772**, 200 (2006).
[5] F. Gelis, E. Iancu, J. Jalilian-Marian, and R. Venugopalan, The color glass condensate, Annu. Rev. Nucl. Part. Sci. **60**, 463 (2010).
[6] J. Berges, K. Boguslavski, S. Schlichting, and R. Venugopalan, Turbulent thermalization process in heavy-ion collisions at ultrarelativistic energies, Phys. Rev. D **89**, 074011 (2014).
[7] J. Berges, K. Boguslavski, S. Schlichting, and R. Venugopalan, Universal attractor in a highly occupied non-Abelian plasma, Phys. Rev. D **89**, 114007 (2014).
[8] C. Scheppach, J. Berges, and T. Gasenzer, Matter-wave turbulence: Beyond kinetic scaling, Phys. Rev. A **81**, 033611 (2010).
[9] B. Nowak, J. Schole, D. Sexty, and T. Gasenzer, Nonthermal fixed points, vortex statistics, and superfluid turbulence in an ultracold Bose gas, Phys. Rev. A **85**, 043627 (2012).
[10] A. Piñeiro Orioli, K. Boguslavski, and J. Berges, Universal self-similar dynamics of relativistic and nonrelativistic field theories near nonthermal fixed points, Phys. Rev. D **92**, 025041 (2015).
[11] J. Berges, K. Boguslavski, S. Schlichting, and R. Venugopalan, Universality Far from Equilibrium: From Superfluid Bose Gases to Heavy-Ion Collisions, Phys. Rev. Lett. **114**, 061601 (2015).

[12] D. Son, Reheating and thermalization in a simple scalar model, Phys. Rev. D **54**, 3745 (1996).
[13] G. Aarts and J. Berges, Classical Aspects of Quantum Fields Far from Equilibrium, Phys. Rev. Lett. **88**, 041603 (2002).
[14] A. Adams, P. Chesler, and H. Liu, Holographic vortex liquids and superfluid turbulence, Science **341**, 368 (2013).
[15] C. Ewerz, T. Gasenzer, M. Karl, and A. Samberg, Non-thermal fixed point in a holographic superfluid, J. High Energy Phys. 05 (2015) 070.
[16] T. Epelbaum and F. Gelis, Role of quantum fluctuations in a system with strong fields: Spectral properties and thermalization, Nucl. Phys. **A872**, 210 (2011).
[17] K. Dusling, T. Epelbaum, F. Gelis, and R. Venugopalan, Instability-induced pressure isotropization in a longitudinally expanding system, Phys. Rev. D **86**, 085040 (2012).
[18] T. Epelbaum and F. Gelis, Pressure Isotropization in High-Energy Heavy-Ion Collisions, Phys. Rev. Lett. **111**, 232301 (2013).
[19] J. Berges, K. Boguslavski, S. Schlichting, and R. Venugopalan, Basin of attraction for turbulent thermalization and the range of validity of classical-statistical simulations, J. High Energy Phys. 05 (2014) 54.
[20] J. Berges, B. Schenke, S. Schlichting, and R. Venugopalan, Turbulent thermalization process in high-energy heavy-ion collisions, Nucl. Phys. **A931**, 348 (2014).
[21] A. Kurkela and Y. Zhu, Isotropization and Hydrodynamization in Weakly Coupled Heavy-Ion Collisions, Phys. Rev. Lett. **115**, 182301 (2015).
[22] T. Epelbaum, F. Gelis, S. Jeon, G. Moore, and B. Wu, Kinetic Theory of a Longitudinally Expanding System of Scalar Particles, J. High Energy Phys. 09 (2015) 117.
[23] J. Berges, K. Boguslavski, S. Schlichting, and R. Venugopalan, Nonequilibrium fixed points in longitudinally expanding scalar theories: Infrared cascade, Bose condensation and a challenge for kinetic theory, Phys. Rev. D **92**, 096006 (2015).
[24] J. Berges, Controlled nonperturbative dynamics of quantum fields out of equilibrium, Nucl. Phys. **A699**, 847 (2002).
[25] G. Aarts, D. Ahrensmeier, R. Baier, J. Berges, and J. Serreau, Far-from-equilibrium dynamics with broken symmetries from the $1/N$ expansion of the 2PI effective action, Phys. Rev. D **66**, 045008 (2002).
[26] J. Berges, Nonequilibrium Quantum Fields: From Cold Atoms to Cosmology, arXiv:1503.02907.
[27] J. Zinn-Justin, *Quantum Field Theory and Critical Phenomena* (Oxford University Press, Oxford, 2002).
[28] M. Alford, J. Berges, and J. Cheyne, Critical phenomena from the two-particle irreducible $1/N$ expansion, Phys. Rev. D **70**, 125002 (2004).
[29] J. Berges and J. Serreau, Parametric Resonance in Quantum Field Theory, Phys. Rev. Lett. **91**, 111601 (2003).
[30] J. Berges and G. Hoffmeister, Nonthermal fixed points and the functional renormalization group, Nucl. Phys. **B813**, 383 (2009).
[31] R. Micha and I. Tkachev, Turbulent thermalization, Phys. Rev. D **70**, 043538 (2004).
[32] J. Berges and D. Sexty, Strong versus weak wave-turbulence in relativistic field theory, Phys. Rev. D **83**, 085004 (2011).
[33] A. Arrizabalaga, J. Smit, and A. Tranberg, Tachyonic preheating using 2PI-$1/N$ dynamics and the classical approximation, J. High Energy Phys. 10 (2004) 017.
[34] G. Aarts and J. Smit, Classical approximation for time-dependent quantum field theory: Diagrammatic analysis for hot scalar fields, Nucl. Phys. **B511**, 451 (1998).
[35] T. Epelbaum, F. Gelis, and B. Wu, Nonrenormalizability of the classical-statistical approximation, Phys. Rev. D **90**, 065029 (2014).
[36] J. Berges, D. Gelfand, and J. Pruschke, Quantum Theory of Fermion Production after Inflation, Phys. Rev. Lett. **107**, 061301 (2011).
[37] J. Berges, D. Gelfand, and D. Sexty, Amplified fermion production from overpopulated Bose fields, Phys. Rev. D **89**, 025001 (2014).
[38] J. Serreau and R. Parentani, Nonperturbative resummation of de Sitter infrared logarithms in the large-N limit, Phys. Rev. D **87**, 085012 (2013).
[39] F. Gautier and J. Serreau, Scalar field correlator in de Sitter space at next-to-leading order in a $1/N$ expansion, Phys. Rev. D **92**, 105035 (2015).
[40] J. Berges and T. Gasenzer, Quantum versus classical statistical dynamics of an ultracold Bose gas, Phys. Rev. A **76**, 033604 (2007).
[41] M. Garny and M. Müller, Kadanoff-Baym equations with non-Gaussian initial conditions: The equilibrium limit, Phys. Rev. D **80**, 085011 (2009).